Available online at www.sciencedirect.com
ScienceDirect
Journal of Catalysis 251 (2007) 69–79
JOURNAL OF CATALYSIS
www.elsevier.com/locate/jcat

Synthesis, characterization, and catalytic properties of hydrothermally stable macro–meso–micro-porous composite materials synthesized via in situ assembly of preformed zeolite Y nanoclusters on kaolin

Qingfeng Tan [a], Xiaojun Bao [a,b,*], Tengchun Song [a], Yu Fan [b], Gang Shi [b], Baojian Shen [b], Conghua Liu [c], Xionghou Gao [c]

[a] *State Key Laboratory of Heavy Oil Processing, China University of Petroleum, No. 18 Fuxue Road, Changping, Beijing 102249, PR China*
[b] *The Key Laboratory of Catalysis, China National Petroleum Corporation, China University of Petroleum, No. 18 Fuxue Road, Changping, Beijing 102249, PR China*
[c] *Petrochemical Research Institute, Lanzhou Petrochemical Company, PetroChina Company, Ltd., Lanzhou 730060, PR China*

Received 2 January 2007; revised 11 July 2007; accepted 13 July 2007

Available online 28 August 2007

Abstract

Hydrothermally stable composite materials with hierarchical macro–meso–micro-porous structure were successfully synthesized via in situ assembly of preformed zeolite Y nanoclusters on kaolin using cetyltrimethylammonium bromide as template under alkaline conditions. The characterization results show that the mesophase in the composite contains primary and secondary structural building units of zeolite Y. The building units contribute micropores in the composite with acidity similar to that of zeolite Y, whereas the macroporous kaolin substrate contributes macropores. This hierarchical macro–meso–micro-porous structure increases the accessibility of the active sites in the composite to reactants and thus confers superior catalytic performance on the resulting catalyst in cracking heavy crude oil. The present work demonstrates that the in situ assembly of zeolitic nanoclusters on substrates (e.g., kaolin) can provide a novel route for fabricating composite materials with hierarchical pore structure.

Keywords: Kaolin; Zeolite Y; Macro–meso–micro-porous composite materials; Hydrothermal stability; Zeolitic nanoclusters; In situ assembly; Catalytic cracking

1. Introduction

Inorganic microporous zeolites with uniform pore size, unique topology, adjustable acidity, and excellent structural stability are widely used in many petrochemical processes. The well-defined micropores (usually <1 nm) of microporous zeolites confer exceptional properties for their applications in various size-selective reaction and separation processes. On the other hand, these relatively narrower pores also put limits on the application of microporous zeolites in the conversion and separation of bulky molecules, such as encountered in heavy crude oil upgrading and organic waste treatment, because of diffusion limitations on chemical reaction and mass transfer [1]. Many approaches to overcoming this shortage of and improving transport in microporous zeolites have been developed, including desilication, dealumination, synthesis of wide-pore zeolites and nanosized zeolites, and carbon-templated synthesis [2]. One of the most effective approaches involves creating the so-called "hierarchical pore structure" by compositing a microporous zeolite and a mesoporous material containing ordered 2–50 nm mesopores [3,4]. For this reason, mesoporous materials have received extensive attention since their emergence in 1992 [5]. Despite numerous efforts over the last 15 years [6–9], the fabrication of mesoporous materials with high hydrothermal stability and adjustable acidity remains one of the greatest challenges in materials science. This is because typical applications of these materials, such as heavy crude oil fluid catalytic cracking (FCC) and hydrocracking, usually involve

* Corresponding author. Fax: +86 0 10 89734979.
E-mail address: baoxj@cup.edu.cn (X. Bao).

0021-9517/$ – see front matter
doi:10.1016/j.jcat.2007.07.014

severe operations that expose the materials to steam at high temperature during reaction or catalyst regeneration.

Recent studies have identified that the poor hydrothermal stability and weak acidity of mesoporous materials are due to the amorphous nature of their pore walls [10]. Therefore, assembling primary and secondary structural building units (nanoclusters or seeds) of microporous zeolites should provide an alternative way to synthesize mesoporous materials with improved thermal and hydrothermal stability and suitable acidity [11–15]. For examples, Pinnavaia's group [11,12] prepared steam-stable aluminosilicates MSUs from the seed solutions of zeolites Y, β, and ZSM-5, and Xiao's group [13–15] prepared hydrothermally stable mesoporous aluminosilicates from preformed zeolite precursors in both alkaline and acidic media. Reportedly, these materials can survive severe treatments, such as in boiling water for more than 300 h and in steam at 800 °C for more than 2 h. In addition to their high hydrothermal stability, these mesoporous materials containing nanoclusters of a zeolitic nature are also marked by a unique pore channel system consisting of mutually interconnected mesopores and micropores (bimodal pore system) [14,15]. This kind of pore system can accelerate the transport of reactant molecules [16]. It differs greatly from the conventional dual-pore structure arising in crystalline composites [17,18] and crystalline mechanical mixtures [19]; the microporous structure existing in crystalline microphases usually has relatively longer diffusion paths [17–19], whereas the microporous channels connected to the more open mesopores in assembled mesostructural materials [14,15] result from zeolitic building units residing in the mesopore walls and thus have much shorter diffusion paths for molecules. This is a significant factor for diffusion-limited reactions [20].

W.R. Grace & Co. [21,22], the former Engelhard Corp. (now acquired by BASF) [23–25], along with some other researchers [26,27] have demonstrated that the bimodal NaY/kaolin FCC catalysts obtained by overgrowing zeolite NaY on metakaolin microspheres has much better catalytic cracking performance, expressed in terms of heavy oil conversion, liquid product yield, dry gas yield, and coke yield, due to the improved accessibility of active sites to bulky heavy oil molecules, enhanced resistance to attrition, high tolerance to contaminant metals, and excellent stability to temperature and steam [28]. Whereas much progress has been achieved on the synthesis of bimodal materials [3,4,17–19,21–27], the synthesis of materials with hierarchical macro–meso–micro-porous structure remains unexplored.

In the present study, novel macro–meso–micro-porous composite materials designated mesoporous Y/kaolin composites or MY/kaolin composites were synthesized via the in situ assembly of preformed zeolite Y nanoclusters on kaolin in an alkaline medium. The composite materials were characterized by X-ray diffraction (XRD), scanning electron microscopy (SEM), transmission electron microscopy (TEM), Fourier transformed infrared spectroscopy (FTIR), N_2 and Ar adsorption isotherms, mercury porosimetry, ^{27}Al magic-angle spinning nuclear magnetic resonance (^{27}Al MAS NMR), and differential scanning calorimetry (DSC). The acidity of the samples was measured by temperature-programmed desorption of ammonia (NH_3-TPD) and in situ IR spectroscopy of adsorbed pyridine (Py-IR). The catalytic properties of the materials were assessed in a microactivity testing (MAT) unit using heavy oil catalytic cracking as a model reaction system.

2. Experimental

2.1. Materials

Sodium silicate (containing 26.0 wt% SiO_2) was purchased from Beijing Hongxing Chemicals Co. Aluminum sulfate (containing 99.0 wt% $Al_2(SO_4)_3{\cdot}18H_2O$) and sodium hydroxide (containing 96.0 wt% NaOH) were purchased from Beijing Yili Fine Chemicals Co. Cetyltrimethylammonium bromide (CTABr) (containing 99.0 wt% $C_{19}H_{42}BrN$) was purchased from Beijing Chemical Reagents Co. Kaolin particles (10–40 μm, containing 37 wt% Al_2O_3 and 48 wt% SiO_2) were kindly provided by Lanzhou PetroChemical Company, PetroChina Company, Ltd.

2.2. Synthesis

The typical synthesis of the MY/kaolin composites involved the following steps:

1. Preformed zeolite Y nanoclusters were prepared by mixing 4.6 g of sodium silicate, 0.9 g of aluminum sulfate, and 1.25 g of sodium hydroxide with 4.8 mL of deionized water while stirring. Then the resulting mixture with a molar ratio of $Na_2O{:}Al_2O_3{:}SiO_2{:}H_2O$ at 16:1.0:15:300 was transferred into an autoclave and dynamically aged at 95 °C for 24 h.
2. The preformed nanocluster solution obtained in step 1 was added dropwise to a solution obtained by dissolving 0.75 g of CTABr in 14.1 mL of deionized H_2O. The pH of the resulting mixture gel was adjusted to 10.5 with a 10% sulfuric acid solution and aged at 45 °C for 12 h.
3. A 0.7 g sample of kaolin particles was mixed with 12.2 mL of 6.0 wt% sodium hydroxide solution containing 4.0 wt% CTABr, and the fresh mixture gel obtained in step 2 was added under agitation. Then the whole reaction system was placed in a rotary autoclave at 120 °C for 36 h.
4. After crystallization, the solid product was filtered, washed with deionized water, dried, and calcined at 550 °C for 6 h in air to remove the organic template, producing the MY/kaolin composite.

This preparation procedure is schematically depicted in Fig. 1.

For comparison purposes, a pure-phase zeolite Y was prepared by statically crystallizing the preformed zeolite Y nanocluster solution at 100 °C for 24 h. Si-MCM-41 and Al-MCM-41 were prepared under the same conditions used for the MY/kaolin composite, except that the nanocluster solution was replaced by corresponding amounts of sodium silicate and aluminate and kaolin particles were not used. Following the same in situ synthesis strategy, two reference composites, Y/kaolin and Y/MCM-41, were obtained for comparison purpose.

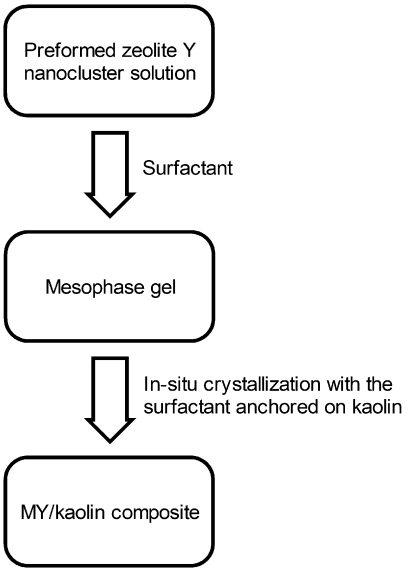

Fig. 1. Schematic of the typical synthesis procedure of a MY/kaolin composite.

2.3. Characterization

The XRD patterns of the samples were obtained on a Shimadzu XRD-6000 diffractometer using nickel-filtered Cu$K\alpha$ X-ray source radiation and operated at 40 kV and 30 mA. After being coated with a thin layer of gold, the samples were evaluated by SEM for a morphology study using a Cambridge S-360 apparatus combined with energy-dispersive X-ray spectrometry (EDS). TEM images were obtained using a JEOL-2000FX II electron microscope operated at 120 kV. The FTIR spectra of the samples were recorded on a Nicolet Magna-IR 560 ESP spectrometer with a resolution of 1 cm^{-1}. N_2 adsorption and desorption isotherms were measured on a Micromeritics ASAP 2020M system at liquid nitrogen temperature. All samples were degassed at 300 °C for 24 h before analysis.

The Brunauer–Emmett–Teller (BET) method was used to calculate the specific surface areas of the samples. The diameter distribution of mesopores and micropores were calculated by Barrett–Joyner–Halenda (BJH) and Horvath–Kawazoe (HK) models, respectively. Mercury porosimetry experiments were carried out on a Micromeritics AutoPoreIV 9500 apparatus in the pressure range 0–30000 psia. Argon adsorption experiments at 77 K were conducted on a Micromeritics ASAP 2020M system in the relative pressure range of 10^{-6}–0.995, and the density functional theory (DFT) model was used to calculate micropore size. ^{27}Al solid-state MAS NMR experiments were performed on a Varian Unity Inova 300 spectrometer equipped with a double-resonance 6-mm Chemagnetics MAS probe and operated at a frequency of 59.59 MHz, a pulse width of 1.5 μs, a radiofrequency field strength of 50 G, a pulse delay of 2 s, a spinning rate of 5 kHz, and 10,000 scans. The DSC analysis was performed on a Netzsch STA409PC thermogravimetric analyzer with a heating rate of 5 °C/min in air. The NH_3-TPD curves were obtained in the range of 100–500 °C at a heating rate of 15 °C/min. The adsorption of ammonia on the samples was performed at room temperature, followed by removing physically adsorbed ammonia at 100 °C for 1 h in flowing pure nitrogen. Pyridine adsorption experiments were conducted on self-supported wafers in an in situ IR cell. Samples were dehydrated at 500 °C for 5 h under a vacuum of 1.33×10^{-3} Pa, followed by adsorption of purified pyridine vapor at room temperature for 20 min. The system was then evacuated at different temperatures, and IR spectra were recorded.

2.4. Catalytic cracking assessment

The catalytic cracking performance assessment of the different materials obtained was carried out in a MAT unit by the pulse method, using a heavy crude oil as feedstock. The composition analyses of the cracking products were carried out with an Angilent gas chromatograph equipped with a flame ionization detector.

Before assessment, the MY/kaolin composites were converted to ReH form by the repeated procedure of successive ion exchanges with 1.0 M NH_4Cl and 0.05 M $La(NO_3)_3$ solutions, followed by calcination at 550 °C for 2 h. The ReH form composites were pressed into pellets, crushed, sieved to 20–40 mesh, and finally steamed before being used as a catalyst. To calculate the mass fraction of the mesophase MY in the composite and use it to prepare the reference catalysts, mechanic mixtures at various proportions of raw kaolin to single mesoporous MY synthesized without using kaolin were prepared, and their XRD profiles were obtained [18]. Then a working curve was obtained by plotting the sum of the integrated intensities of the three diffraction peaks in the (100), (110), and (200) directions versus the proportion. Using this working curve, the mass fraction of the mesophase MY in the MY/kaolin composite was calculated to be about 50%. For comparison purposes, four reference catalysts (Y-kaolin, Y/kaolin, Y/MCM-41, and Y-MCM-41-kaolin) were prepared according to this ratio. The Y-kaolin and Y-MCM-41-kaolin catalysts were obtained by mechanically blending zeolite Y and kaolin and zeolite Y, Si-MCM-41, and kaolin, respectively. The two reference composites Y/kaolin and Y/MCM-41 were posttreated under the identical conditions used for the MY/kaolin-derived catalyst to obtain the corresponding catalysts.

The heavy crude oil feedstock used was a blend of 30 wt% Xinjiang vacuum residue and 70.0 wt% Xinjiang vacuum gas oil. The physical and chemical properties of the feedstock are given in Table 1. The catalytic cracking was performed under standard conditions. The catalyst loading was 4.0 g, and the reaction temperature was 500 °C; 1.3 g of the heavy crude oil was introduced to the reactor through an injection tube within 60 s, followed by nitrogen purging for 5 min. Before entering the reactor, the feedstock was preheated to 90 °C to improve its flowability. The products were collected in a gas collector and a liquid collector, respectively, through a cooling bath.

3. Results and discussion

3.1. XRD

Fig. 2 shows the XRD patterns of the calcined composite sample before and after the treatment in boiling water for 120 h

Table 1
Properties of the heavy crude oil feed

Item	Property
Density (20 °C) (g/cm^3)	0.885
Viscosity at 100 °C (mm^2/s)	9.518
Conradson carbon residue (m%)	15.80
Initial boiling point (°C)	2.70
Item	223
5% distillation temperature (°C)	278
10% distillation temperature (°C)	315
30% distillation temperature (°C)	372
50% distillation temperature (°C)	430
Element composition (m%)	
C	86.13
H	12.94
N	0.25
S	0.38

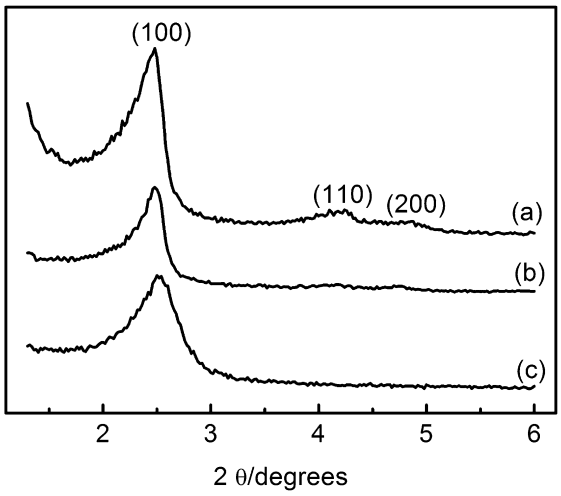

Fig. 2. The small-angle XRD patterns of the calcined composite before (a), after treatment in boiling water for 120 h (b), and after treatment in 100% water vapor at 800 °C for 2 h (c).

and after the treatment in 100% water vapor at 800 °C for 2 h. In the low-angle region from 1.0 to 6.0°, the three distinct diffraction peaks on curve (a) in Fig. 2, indexed as (100), (110), and (200) and associated with hexagonal symmetry, are those specific to the mesoporous structure. They demonstrate the existence of ordered hexagonal mesophase in the composite. In the high-angle range from 10 to 40°, no diffraction peaks are observed, indicating the absence of bulky zeolite phase. The

Table 2
Textural parameters of the Si-MCM-41 and MY/kaolin composite

Samples	d_{100} (nm)	Mesopore diameter (nm)	Wall thickness[a] (nm)	Surface area (m^2/g)	Pore volume (cm^3/g)	Micropore volume (cm^3/g)
Si-MCM-41	3.25	2.74	1.01	1130	0.96	0
MY/kaolin composite	3.86	2.44	2.02	364	0.47	0.10
MY/kaolin composite treated[b]	3.69	2.63	1.64	268	0.36	0.04

[a] The wall thickness was calculated as: a_0—mesopore diameter ($a_0 = 2 \times d_{100}/3^{1/2}$).
[b] In 100% water steam at 800 °C for 2 h.

value of d_{100}, the interplanar spacing in the (100) direction of the mesophase of the calcined composite is 3.86 nm, much larger than that (3.25 nm) of the pure Si-MCM-41 phase prepared under the same conditions, as shown in Table 2. The pore diameters of the mesophase in the MY/kaolin composite and the pure-phase Si-MCM-41 are 2.44 and 2.74 nm, respectively, and the pore wall of the former is 1.0 nm thicker than that of the latter. This can be ascribed to the larger spatial volume and stronger rigidity of the zeolite Y nanoclusters compared with the nonstructured silicon species in the conventional Si-MCM-41 phase [13–15]. After the treatment in boiling water for 120 h [curve (b) in Fig. 2] and in 100% water steam at 800 °C for 2 h [curve (c) in Fig. 2], the mesophase in the composite retains its regular mesoporous structures. These results suggest that the mesophase in the MY/kaolin composite is hydrothermally stable even at high temperatures. In contrast, after hydrothermal treatment in 100% water steam at 800 °C for 2 h, the pure phase Si-MCM-41 loses its mesoporous structure. The better hydrothermal stability of the composite may be due, at least in part, to its zeolite-like connectivity and thicker mesopore wall [29].

3.2. SEM

Fig. 3 displays the SEM images of kaolin microspheres (a), the MY/kaolin composite (b), and the interphase section in the composite (c). From Fig. 3, it can be seen that the MY crystals are evenly and densely packed on the surface of kaolin microspheres. In Fig. 3b, the MY mesophase shows consistent color depth, indicating that no other crystals, such as zeolite Y crystals, are formed [17,30]. By sectioning the composite,

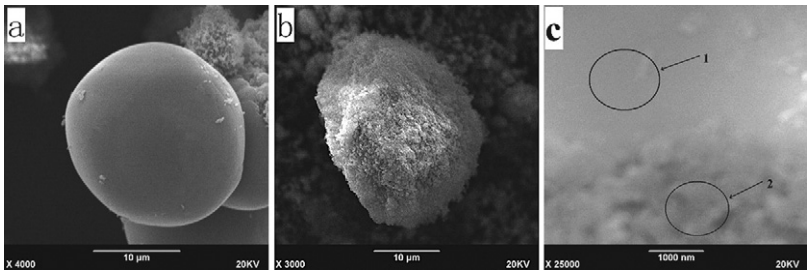

Fig. 3. SEM images of the samples: (a) kaolin particles; (b) calcined composite; (c) the interphase section in the composite.

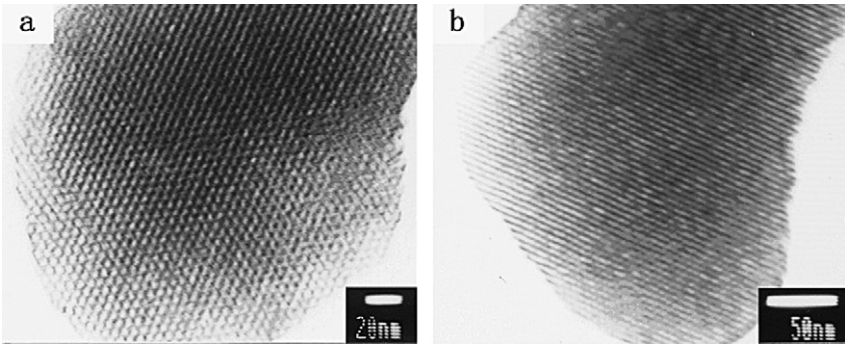

Fig. 4. TEM images of the MY phase in the calcined composite: (a) in the (100) direction; (b) in the (110) direction.

we can see two distinct texture regions (Fig. 3c): the core region (region 1), which is relatively compact, and the shell region (region 2), which is relatively loose. More interestingly, the EDS analysis of the element compositions of the two regions showed that the molar SiO_2/Al_2O_3 ratios of regions 1 and 2 are 2.7 and 15.8, respectively, close to those of the starting kaolin microspheres (2.2) and the initial nanocluster solution (15.0). Moreover, the interface between regions 1 and 2 is difficult to distinguish, suggesting that the MY mesophase is linked to the kaolin phase by chemical bonding. Such chemical-bonding linkage between the MY mesophase and the kaolin phase can greatly increase the thermal and hydrothermal stability of the composite [26,27]. From these results, it can be concluded that the MY mesophase in the composite is certainly overgrown on kaolin microspheres; that is, a core/shell structure is formed. Thus, the composite is undoubtedly not a physical mixture of kaolin and MY. The similar SiO_2/Al_2O_3 molar ratio in the MY mesophase (15.8) in the composite and the initial solution (15.0) of the preformed zeolite Y nanoclusters also indicates that most of the silicon and aluminum species in the initial solution had been incorporated into the MY mesophase during the assembly procedure [14].

3.3. TEM

The TEM images of the MY mesophase in the (100) and (110) directions (Fig. 4) show that the MY mesophase has ordered hexagonal arrays of uniform mesopores. From the TEM images of the calcined samples, the distance between mesopores, the wall thickness, and the size of the mesopores are estimated to be about 4.5, 2.0 and 2.5 nm, respectively. These results are consistent with those from the XRD analyses.

3.4. FTIR

The FTIR spectra of the MY/kaolin composite are shown in Fig. 5. The spectra of the MY/kaolin have two broad bands at about 460 and 800 cm^{-1} [curve (a) in Fig. 5], representing the deformational vibration and symmetric vibration of Si–O bonds, respectively. Another band at about 579 cm^{-1} [curve (a) in Fig. 5], typically ascribed to the double six-member rings in microporous zeolite type Y [31], is also observed, suggesting the presence of primary and secondary structural building units of zeolite Y. These results are consistent with those reported in the literature [32,33]. However, the band characterizing the vibration of the double rings is at 573 cm^{-1} [curve (b) in Fig. 5] for the pure-phase Y zeolite prepared from the same nanocluster solution. This difference infers that the two materials may have different local structural environments in the primary and second structural building units. In fact, it is widely accepted that the array of silicon and aluminum atoms is of long-range order in pure-phase Y zeolite, but not in pure mesophase (e.g., MCM-41) [10].

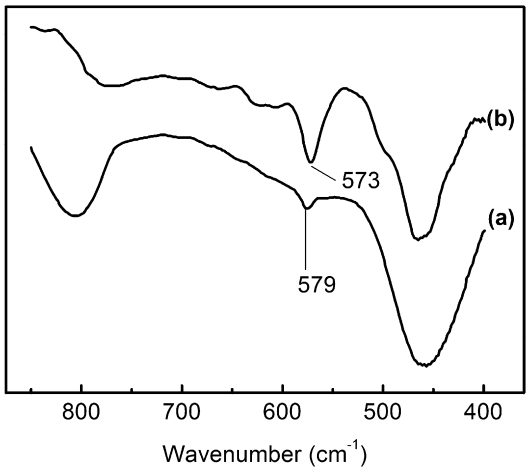

Fig. 5. FT-IR spectra of (a) the calcined composite and (b) the pure phase zeolite Y.

3.5. Pore structure

The N_2 adsorption–desorption technique is considered more effective for assessing the hydrothermal stability of mesostructured materials, because N_2 adsorption–desorption measurements are more sensitive to the structural changes that may occur during hydrothermal treatment. The N_2 adsorption–desorption isotherms of the calcined MY/kaolin composite before and after the treatment in 100% water vapor at 800 °C for 2 h are shown in Fig. 6A; for comparison purposes, the N_2 adsorption–desorption isotherms of Si-MCM-41 (c), zeolite Y (d), and kaolin (e) are shown in Fig. 6B. The isotherm of the calcined composite [curve (a)] shows the representative characteristics of type IV and type I adsorption–desorption. A steep increase in adsorption volume for the composite occurs at relative pressure $P/P_0 < 0.01$, which is not observed

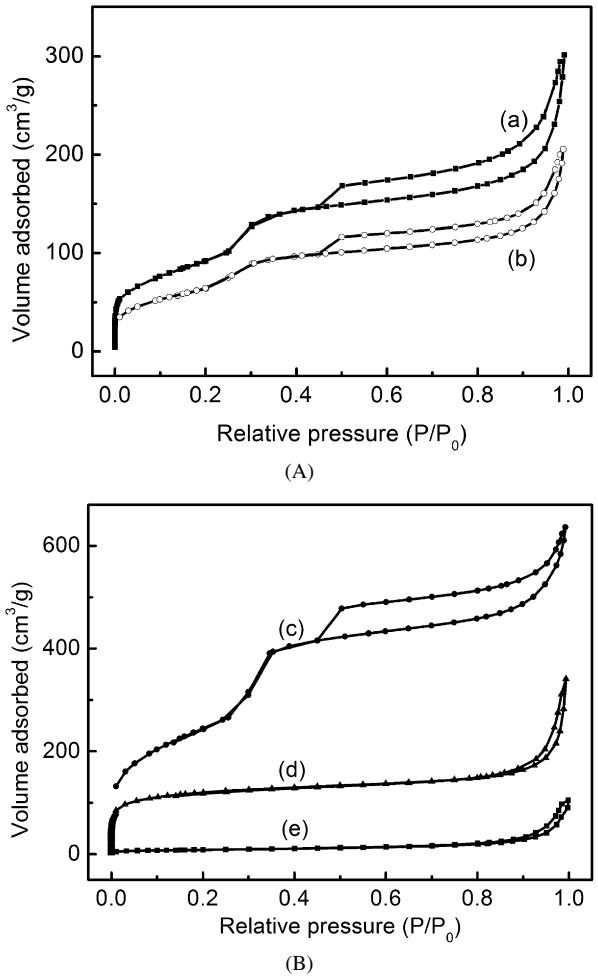

Fig. 6. N_2 adsorption and desorption isotherms of the samples: (A) the calcined composite before (a) and after (b) the hydrothermal treatment in 100% water vapor at 800 °C for 2 h; (B) Si-MCM-41 (c), zeolite Y (d), and kaolin (e).

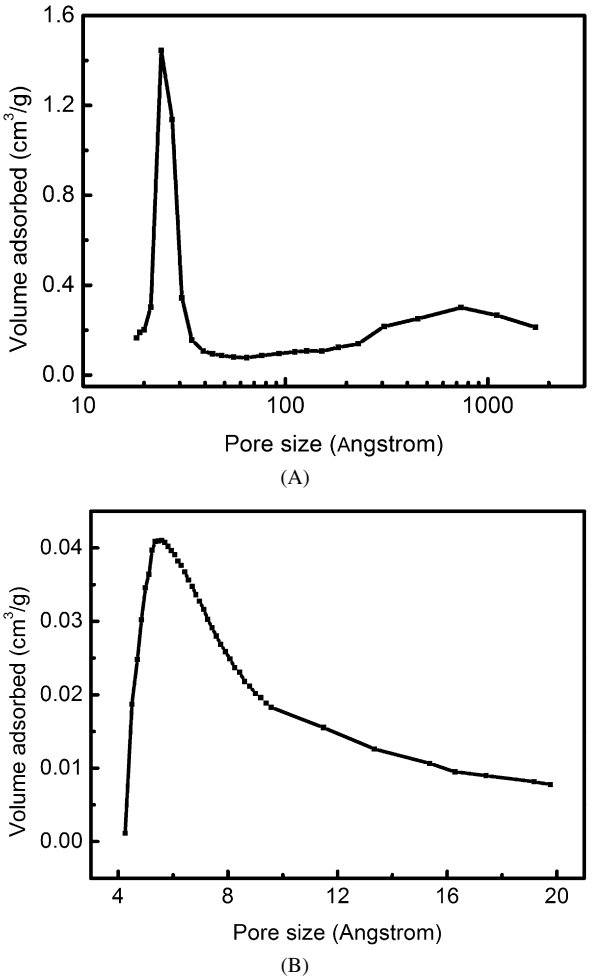

Fig. 7. Pore size distribution of the calcined composite: (A) BJH mesopore; (B) HK micropore.

for either the pure-phase Si-MCM-41 [curve (c) in Fig. 6B] or the kaolin [curve (e) in Fig. 6B]. This indicates that micropores are present in the composite due to the incorporation of primary and secondary structural building units of zeolite Y into the MY mesophase. These incorporated building units behave like microporous zeolite [curve (d) in Fig. 6B] [15]. Another sharp inflection for the composite appears at P/P_0, ranging from 0.25 to 0.40, due to capillary condensation of the adsorbate in the mesoporous structure. The hysteresis loop occurring in the pressure range $0.45 < P/P_0 < 1.0$ is due to the presence of the macropores from the kaolin and interparticle mesopores. These results demonstrate that the MY/kaolin composite obtained has a trimodal macro–meso–micro-porous structure.

The N_2 adsorption–desorption isotherm of the calcined composite after the treatment in 100% water vapor at 800 °C for 2 h exhibits features typical of type IV isotherms [curve (b) in Fig. 6A]. After treatment, the composite retains 74% of the pretreatment surface area and 77% of the pretreatment framework pore volume of the composite (Table 2). These findings are consistent with the XRD analysis results and further confirm the excellent hydrothermal stability of the composite.

Fig. 7 shows the mesopore and micropore size distributions of the calcined composite calculated by the BJH and HK models, respectively. It shows uniform mesopores and micropores narrowly distributed at about 2.5 and 0.56 nm, respectively. As shown in Fig. 7A, a broad distribution is also observed in the pore diameter range >20 nm, signifying the existence of macropores. This further confirms the hierarchical pore structure of the composite. The calculated size of mesopores is in agreement with that estimated from the TEM images shown in Fig. 4. The micropores in the MY/kaolin composite are smaller than the pore channels of ordinary zeolite Y crystals (0.56 nm vs. 0.74 nm), possibly because the pore wall of the mesophase in the composite is not thick enough to accommodate a whole zeolite crystal cell [14]. By the t-plot method, it is estimated that the contribution of the microporous structure to the total pore volume is about 0.10 cm^3/g from N_2 adsorption, as shown in Table 2.

To reaffirm the hierarchy of the pore structures of the composite MY/kaolin, mercury porosimetry and argon sorption measurements were also carried out. The mercury intrusion–extrusion isotherms (Fig. 8A) clearly show an intrusion uptake correlated with the mercury filling in macroporosity. The derived pore size distribution (Fig. 8A) manifestly reveals the

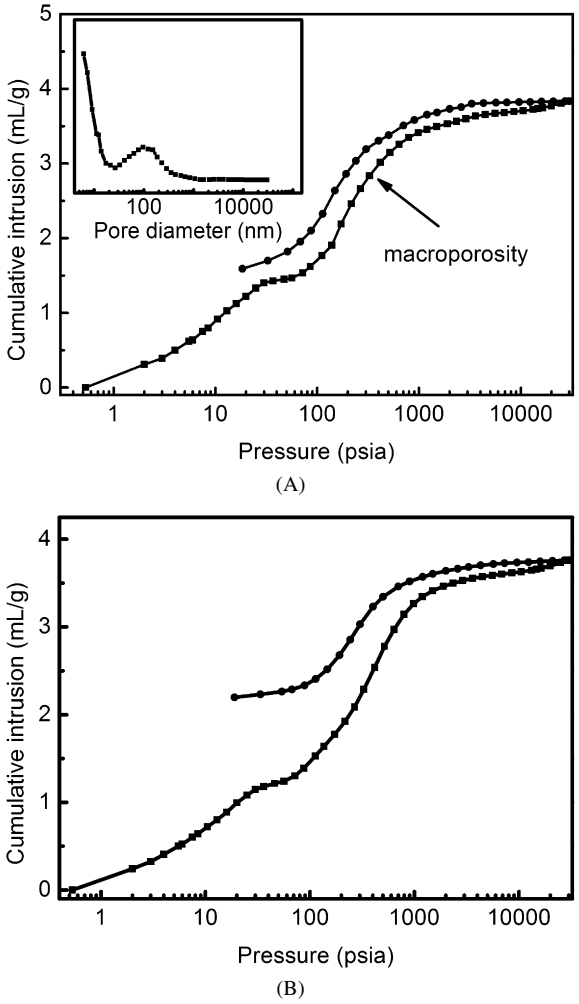

Fig. 8. Mercury intrusion-extrusion isotherms: (A) the composite MY/kaolin; (B) the mechanical mixture of MY and kaolin.

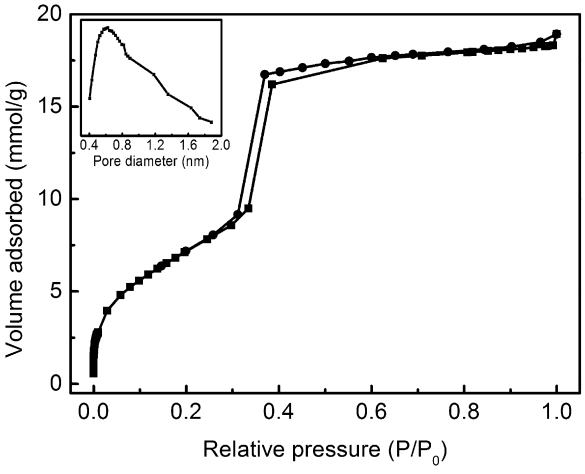

Fig. 9. Argon adsorption–desorption isotherms and the derived DFT micropore size distribution of the composite MY/kaolin.

presence of both macroporous and mesoporous architecture in the composite MY/kaolin. The argon adsorption–desorption isotherms and the derived DFT micropore size distribution are shown in Fig. 9. The argon isotherms of the composite MY/kaolin exhibit a typical IV curve with capillary condensation within the relative pressure range of $0.30 < P/P_0 < 0.40$, which is analogous to the aforementioned nitrogen sorption properties, indicating the presence of the ordered mesoporous structures. More interestingly, the DFT micropore size distribution at 0.62 nm (Fig. 9) is close to the HK micropore size value (0.56 nm) derived from the nitrogen adsorption–desorption measurements. Combining the nitrogen and argon adsorption–desorption results, we can conclude that a hierarchically macro–meso–micro-porous system is undoubtedly established in the composite MY/kaolin.

In hierarchically porous materials, the connectivity of pores of different sizes is significant in terms of their catalytic applications from the standpoint of accessibility. To investigate the macro–meso–micro-pore interconnectivity in the composite MY/kaolin, a mechanical mixture of MY and kaolin with the same mass fraction as that in the composite MY/kaolin was prepared and characterized by mercury porosimetry measurements (Fig. 8B). Comparing Figs. 8A and 8B reveals that the deviation of the extrusion branch from the intrusion branch for the composite MY/kaolin is much less than that for the mechanical mixture, indicating the much lower mercury entrapment during the extrusion process and better accessibility of the framework porosity of the former, that is, higher connectivity between mesopores and macropores for the composite MY/kaolin [34]. In contrast, isolated pores or cavities with lower interconnectivity often lead to negligible mercury intrusion and hold mercury reservation during the extrusion. Because adsorption–desorption hysteresis is related to the accessibility of the gas condensed in a given pore to the surrounding gas phase (i.e., to the connectivity of pores [35]), the negligible adsorption–desorption hysteresis in the argon sorption for the composite MY/kaolin (Fig. 9) suggests that the mesopores of the composite MY/kaolin are entirely accessible from outside and well connected with each other.

Because the foregoing XRD and SEM analysis results confirm the absence of bulky microporous zeolite phase in the composite, and the SEM analyses show that the composite MY/kaolin is composed of kaolin phase and MY mesophase in nature, the microporous structure in the composite MY/kaolin revealed by the FTIR and N_2 and Ar adsorption analysis results is thought to derive exclusively from the mesophase MY due to the absence of microporous structure in kaolin, as shown by curve (e) in Fig. 6B; that is, the microporous structure exists in the mesoporous structure. Because the mesophase MY is overgrown on kaolin microspheres (see Fig. 3), the mesophase is naturally connected to the macropores in the kaolin phase, consistent with the foregoing mercury porosimetry analyses. Thus, a hierarchical macro–meso–micro-pore structure is surely obtained. A schematic representation of the composite MY/kaolin given in Fig. 10 provides more information on the hierarchical pore structure.

Because the wall thickness of the mesophase MY is much smaller than the size of an ordinary zeolite Y crystal, the micropore channels in the MY/kaolin composite (see Fig. 7B) should be much shorter than those in the ordinary zeolite Y crystals. Such an interconnected pore system differs greatly from those

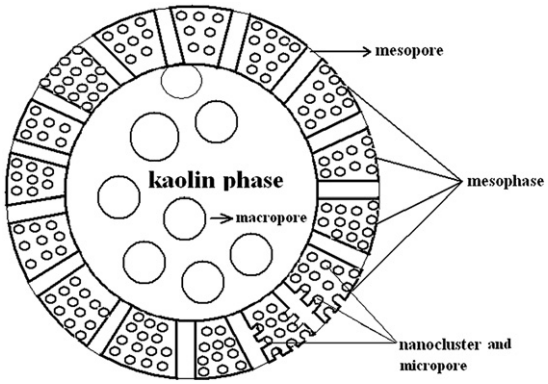

Fig. 10. Schematic representation of envisaged core/shell section structure of the composite MY/kaolin.

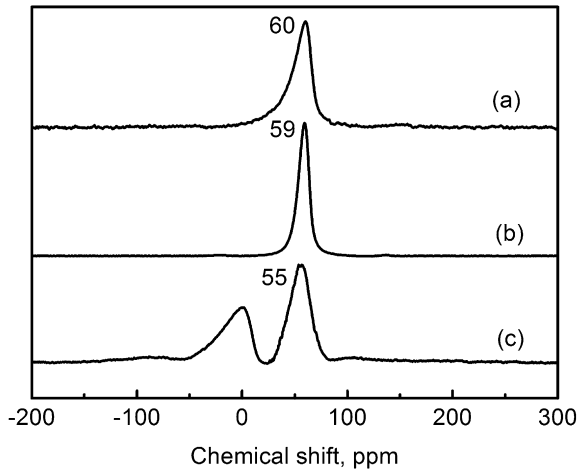

Fig. 11. ^{27}Al NMR spectra of the mesophase MY in the calcined MY/kaolin composite (a), pure-phase zeolite Y (b), and Al-MCM-41 (c).

of the kaolin/NaY/MCM-41 composites synthesized by the two-stage method and the mechanical mixtures of kaolin, NaY, and MCM-41 [36]. This unique pore system should greatly enhance the accessibility of the catalytically active sites inside the microporous channels to larger reactant molecules, accelerate the diffusion of products, and reduce secondary reactions.

3.6. ^{27}Al NMR

The state of Al in the MY mesophase of the calcined composite was studied by ^{27}Al MAS NMR; the results are shown in Fig. 11. The only chemical shift assigned to tetrahedrally coordinated Al species in the framework is at 60 ppm (Fig. 11, curve (a)), which is very close to the 59-ppm shift of those in the pure-phase Y zeolite (Fig. 11, curve (b)) and significantly different from the 55-ppm shift of those in Al-MCM-41 prepared under identical conditions (Fig. 11, curve (c)). This finding suggests that Al species in both the mesophase MY and the pure-phase Y zeolite have a close to similar environment. In contrast, the Al species in Al-MCM-41 after calcination often show an additional chemical shift signal related to the nonframework Al species (Fig. 11, curve (c)) [37]. No visible difference in chemical shift was observed between the as-synthesized samples and

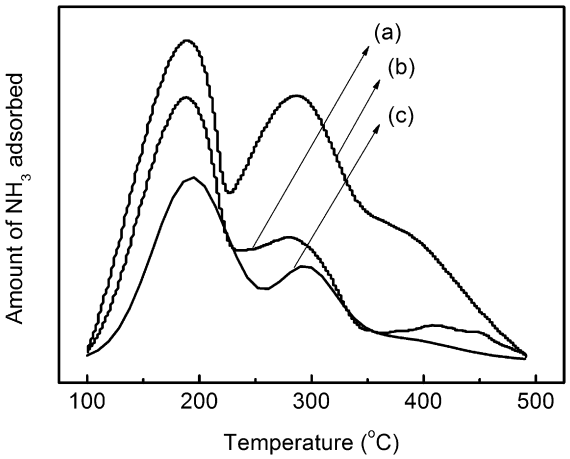

Fig. 12. NH_3-TPD curves of (a) the calcined composite, (b) Y, and Al-MCM-41 (c).

Table 3
Acidic properties of the samples determined by NH_3-TPD technique

Samples	Acidity (mmol NH_3/g solid)			
	Weak acid	Medium acid	Strong acid	Total amount
MY/kaolin	0.333 (58.3%)	0.161 (28.2%)	0.077 (13.5%)	0.571
Zeolite Y	0.377 (40.9%)	0.190 (20.6%)	0.354 (38.4%)	0.921
Al-MCM-41	0.274 (70.5%)	0.098 (25.3%)	0.016 (4.2%)	0.388

the calcined samples, again indicating that the Al species in the framework are stable.

3.7. Acidity

Fig. 12 shows the NH_3-TPD curves of the calcined composite, pure-phase zeolite Y, and Al-MCM-41. The samples had been transformed into protonated form by ion exchange before measurement. Apparently, both the composite (Fig. 12, curve (a)) and the pure-phase zeolite Y (Fig. 12, curve (b)) have three desorption peaks at 190, 286, and 398 °C, corresponding to weak, medium, and strong acid sites, respectively. Al-MCM-41 (Fig. 12, curve (c)) shows only the two former desorption peaks, demonstrating that Al-MCM-41 obtained in the present investigation has only weak and medium acidity, with almost no strong acidity. This indicates that the acidic property of the composite MY/kaolin is similar to that of zeolite Y, but different from that of Al-MCM-41. The acidity of aluminum-containing zeolite catalysts is often influenced by the local environment of Al atoms. As discussed above, the local environment of Al atoms and the pore wall structure in the MY mesophase of the MY/kaolin composite are very similar to those in zeolite Y. The NH_3-TPD results show that the MY mesophase assembled from the preformed zeolite Y nanoclusters accounts for the acidity, especially for the strong acidity of the composite. However, the composite has less total acid sites than the pure-phase Y zeolite, as shown in Table 3. The results in Table 3 also demonstrate that compared with zeolite Y, the MY/kaolin composite has higher percentages of weak and medium acid sites and a lower percentage of strong acid sites. For some acid-catalyzed reactions, such as heavy crude oil cat-

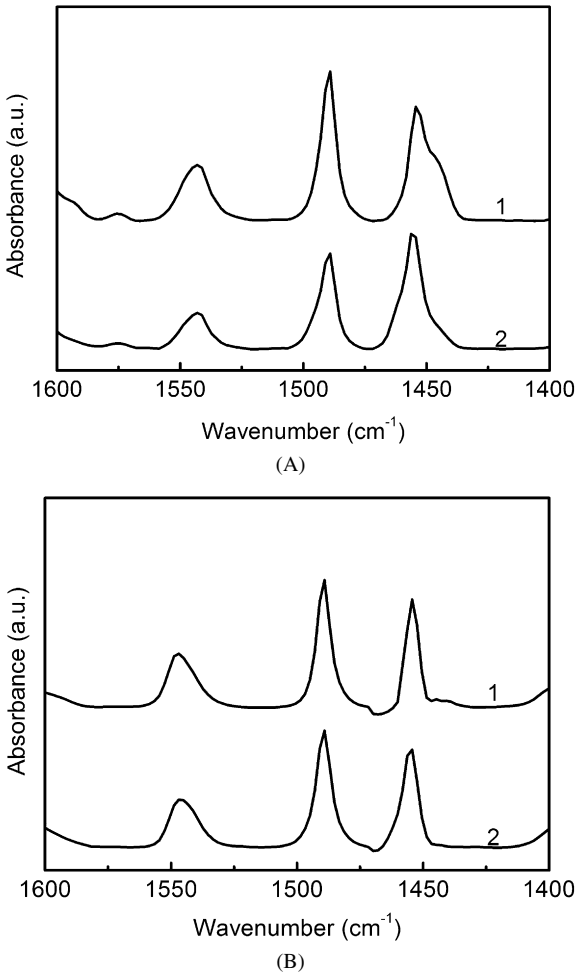

Fig. 13. IR spectra of pyridine adsorbed at 200 °C (curve 1) and 350 °C (curve 2): (A) protonated composite; (B) protonated pure phase zeolite Y.

Table 4
Acidic properties of the calcined composite and the pure phase zeolite Y

Samples	Acidity (A cm^2/g)					
	Brönsted		Lewis		Total	
	200 °C	350 °C	200 °C	350 °C	200 °C	350 °C
Composite	12.0	6.9	25.3	16.3	37.3	23.2
Pure phase zeolite Y	20.8	8.2	42.7	26.0	63.5	34.2

alytic cracking, the weaker acidity may mean relatively lower catalytic activity.

IR spectroscopy of adsorbed pyridine is another technique for measuring and distinguishing different types of acid sites on zeolite surfaces. The IR spectra of pyridine adsorbed on the protonated samples of the composite and the pure-phase Y zeolite in wavenumber region 1600–1400 cm^{-1} are presented in Fig. 13. The two bands at 1540 and 1450 cm^{-1} are related to the adsorption of pyridine molecules on Brönsted and Lewis acid sites, respectively. Table 4 lists the acid strength distributions of the composite and the pure-phase Y zeolite quantitatively calculated from the results of pyridine adsorbed IR spectra at 200 and 350 °C. At the two thermal desorption temperatures, there are less Brönsted acid sites and Lewis acid sites in the composite than in the pure-phase Y zeolite. This is in agreement with the NH_3-TPD characterization results. The acidity measurement results verify the zeolite-like structural characteristics of the mesophase MY in the MY/kaolin composite.

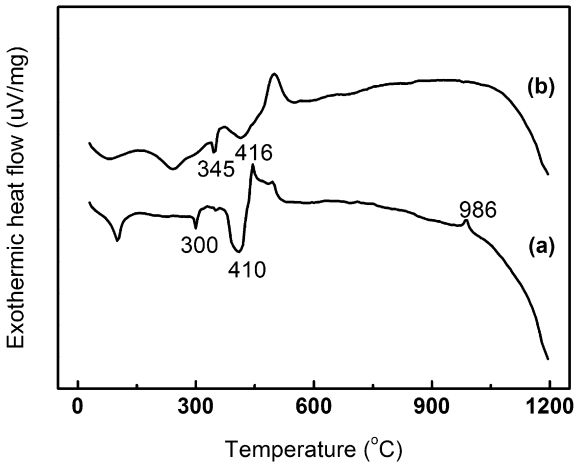

Fig. 14. DSC curves of (a) the composite and (b) Si-MCM-41.

3.8. DSC

The DSC analysis results of the composite and Si-MCM-41 are shown in Fig. 14. The two peaks on curve (a) for the composite at 300 and 410 °C can be assigned to the desorption and decomposition temperatures of the template CTABr in the mesophase MY, respectively, both of which are below 345 and 416 °C on curve (b), the corresponding desorption and decomposition temperatures of CTABr in the pure-phase Si-MCM-41. The easier thermal desorption and decomposition of CTABr in the mesophase MY is an indication of the weaker interaction between CTABr and the mesopore walls in the composite [18,37]. Fig. 14 also shows that the exothermal peak representing the transformation of kaolin phase to mullite phase shifts from 994 °C for the kaolin spheres to 986 °C for the composite, due to the decreased structural integrity of the kaolin phase after the overgrowth of the mesophase MY [38], because the surface part of kaolin spheres is dissolved into the liquid gel and participate in formation of the MY mesophase. The presence of the kaolin phase in the composite further confirms the macro–meso–micro-porous structure of the composite, in which the retained kaolin provides macropores. Kaolin in the composite, functioning as a substrate, also can contribute to the excellent hydrothermal stability of the composite [27].

3.9. Catalytic properties

To explore the potential of the MY/kaolin composite as a catalyst, the catalytic performance of the MY/kaolin composite-derived catalyst was tested for cracking heavy crude oil and compared with that of the Y-kaolin-, Y/kaolin-, Y/MCM-41-, and Y-MCM-41-kaolin-derived catalysts. The results are listed in Table 5. Among the five catalysts, the MY/kaolin-derived one shows the lowest dry gas yield (1.5 wt%) and a very low coke yield (6.9 wt%). As is well known, the dry gas and

Table 5
Catalytic cracking results of the different catalysts

Samples	Yield (wt%)						
	Dry gas	LPG (C_3+C_4)	Gasoline	Diesel	HCO	Coke	Gasoline + diesel
MY/kaolin	1.5	10.8	43.8	30.6	6.4	6.9	74.4
Y-kaolin	2.5	12.9	39.6	28.5	7.9	8.7	68.1
Y/kaolin	2.7	13.1	40.8	28.4	6.6	8.4	69.2
Y/MCM-41	1.9	12.1	43.2	29.4	7.3	6.1	72.6
Y-MCM-41-kaolin	2.2	13.5	41.8	29.3	6.0	7.2	71.1

coke come from the secondary reactions, because of the limited outward diffusion of the product molecules. It also was found that the diffusion coefficient of molecules in mesopores is several orders of magnitude larger than that in micropores, which are close in size to the molecules involved [20]. Therefore, the lower yields of dry gas and coke over the composite MY/kaolin derived catalyst can be attributed, at least in part, to the presence of mesopores in the composite. Such an explanation is further supported by comparing the catalytic behavior of the mesophase-containing catalysts (Y/MCM-41 and Y-MCM-41-kaolin) and the mesophase-free catalysts (Y-kaolin and Y/kaolin); the former two catalysts show lower yields of dry gas and coke (Table 5). This is because the mesopores in the catalysts can accelerate the diffusion of the product molecules, and thus the secondary reactions leading to dry gas and coke formation are decreased [39]. For hydrocarbon transformation over zeolite materials, conversion and selectivity are largely influenced by the time that the hydrocarbon molecules spend inside the zeolitic micropores [20]. As discussed before, the micropore channels in the composite MY/kaolin are much shorter than those in pure-phase zeolite Y crystals and thus help decrease unwanted secondary reactions that lead to massive formation of dry gas and coke. This interpretation is perfectly in line with the concept of pore continuum [40], which states that essentially, a product molecule that diffuses outward the zeolitic micropores will spend less time within the zeolitic micropores and thus will have less chance to undergo the resulting secondary cracking reaction if the zeolitic micropores are short and the mouth of the zeolitic micropores is in close contact with mesopores. For the same reason, the dry gas and coke yields of the composite MY/kaolin-derived catalyst are also lower than those of the Y/MCM-41- and Y-MCM-41-kaolin-derived catalysts (Table 5), whereas the latter two catalysts also have regular mesopores. This is because the microporous phase (zeolite Y) in the latter two catalysts exists in the bulk-phase form; that is, the micropores in Y/MCM-41 and Y-MCM-41-kaolin are relatively longer than those in the composite MY/kaolin.

Surprisingly, the composite MY/kaolin-derived catalyst also gives the highest yield of light fraction oil (gasoline + diesel) among the five catalysts, even though the composite MY/kaolin is of lower acidity than zeolite Y. These results are consistent with but better than those reported by Kloetstra [17], who reported that MCM-41-coated USY gave 4.5 wt% higher selectivity to lighter fractions than the original USY for cracking vacuum gasoil. In fact, it is widely accepted that catalyst acidity is not the only factor determining conversion and product distribution and that the accessibility of catalytically active sites often plays a critical role in some diffusion-controlled reactions [41,42]. Therefore, the higher light fraction yield of the composite MY/kaolin-derived catalyst compared with the other catalysts should be attributed to the enhanced accessibility of active sites to reactant molecules thanks to the unique macro–meso–microporous structure. This is because in the hierarchical pore structure of the composite MY/kaolin, the reactant molecules are first transported through the mesopores and then adsorbed in micropores to undergo shape-selective catalytic cracking reactions [43]. Thus, precracking of the feedstock molecules in the mesopores before they enter the zeolitic micropores results in the higher gasoline yields in the final product distribution (Table 5) [41]. Here we can infer that the enhanced accessibility to active sites, induced mainly from the mesopores of the hierarchical pore structure, can partially compensate for the relatively lower acidity of the composite MY/kaolin-derived catalyst [39], as can be seen from the higher light fraction yields of the mesopore-containing catalysts (Y/MCM-41 and Y-MCM-41-kaolin) compared with the mesopore-free catalysts (Y-kaolin and Y/kaolin) (Table 5).

The foregoing catalytic results fully demonstrate that the hierarchical macro–meso–micro-porous structure of the MY/kaolin composite can significantly facilitate molecule diffusion and increase the accessibility of the acid sites located in microporous channels to larger reactant molecules.

4. Conclusion

In this study, MY/kaolin composites with hierarchical macro–meso–micro-porous structure were synthesized for the first time via the overgrowth of ordered mesophase MY on kaolin spheres through the in situ assemblage of preformed zeolite Y nanoclusters. The characterization results for the composites show that they have high hydrothermal stability, moderate acidity, and an advantageous pore system comprising micropores, mesopores, and macropores. The mesophase MY in the MY/kaolin composites contains primary and secondary structural building units of zeolite Y and contributes the shorter micropores and moderate acidity, whereas the macropores in the composite are inherited mainly from kaolin. The unique pore structure of the composites significantly facilitates mass transfer and greatly increases the accessibility to catalytically active sites in microporous channels. As a result, the composite-derived catalysts perform excellently in heavy crude oil cracking. The methodology introduced in this study provides a novel route for preparing composite materials with hierarchical pore

structure that have wide applications in catalysis reactions, especially those involving conversion of bulky molecules.

Acknowledgments

Financial support was provided by the Ministry of Science and Technology of China through the National Basic Research Program (grant 2004CB217807).

References

[1] M.J. Verhoef, P.J. Kooyman, J.C. van der Waal, M.S. Rigutto, J.A. Peters, H. van Bekkum, Chem. Mater. 13 (2001) 683.
[2] J.C. Groen, J.A. Moulijn, J. Perez-Ramirez, J. Mater. Chem. 16 (2006) 2121.
[3] M. Ogura, S. Shinomiya, J. Tateno, Y. Nara, E. Kikuchi, M. Matsukata, Chem. Lett. 29 (2000) 882.
[4] C.J.H. Jacobsen, C. Madsen, J. Houzvicka, I. Schmidt, A. Carlsson, J. Am. Chem. Soc. 122 (2000) 7116.
[5] J.S. Beck, J.C. Vartuli, W.J. Roth, M.E. Leonowicz, C.T. Kresge, K.D. Schmitt, C.T.-W. Chu, D.H. Olson, E.W. Sheppard, S.B. McCullen, J.B. Higgins, J.L. Schlenkert, J. Am. Chem. Soc. 114 (1992) 10834.
[6] R. Ryoo, S. Jun, J. Phys. Chem. B 101 (1997) 317.
[7] R. Mokaya, W. Jones, Chem. Commun. 17 (1998) 1839.
[8] S.S. Kim, W. Zhang, T.J. Pinnavaia, Science 282 (1998) 1032.
[9] D. Zhao, J. Feng, Q. Huo, N. Melosh, G.H. Fredrickson, B.F. Chmelka, G.D. Stucky, Science 279 (1998) 548.
[10] A. Corma, Chem. Rev. 97 (1997) 2373.
[11] Y. Liu, W. Zhang, T.J. Pinnavaia, J. Am. Chem. Soc. 122 (2000) 8791.
[12] Y. Liu, W. Zhang, T.J. Pinnavaia, Angew. Chem. Int. Ed. 40 (2001) 1255.
[13] Z. Zhang, Y. Han, L. Zhu, R. Wang, Y. Yu, S. Qiu, D. Zhao, F. Xiao, Angew. Chem. Int. Ed. 40 (2001) 1258.
[14] Y. Han, S. Wu, Y. Sun, D. Li, F. Xiao, J. Liu, X. Zhang, Chem. Mater. 14 (2002) 1144.
[15] Z. Zhang, Y. Han, F. Xiao, S. Qiu, L. Zhu, R. Wang, Y. Yu, Z. Zhang, S. Zou, Y. Wang, H. Sun, D. Zhao, Y. Wei, J. Am. Chem. Soc. 123 (2001) 5014.
[16] C.G. Goltner, B. Smarsly, B. Berton, M. Antonietti, Chem. Mater. 13 (2001) 1617.
[17] K.R. Kloetstra, H.W. Zandbergen, J.C. Jansen, H. van Bekkum, Microporous Mater. 6 (1996) 287.
[18] L. Huang, W. Guo, P. Deng, Z. Xue, Q. Li, J. Phys. Chem. B 104 (2000) 2817.
[19] W. Guo, L. Huang, P. Deng, Z. Xue, Q. Li, Microporous Mesoporous Mater. 44–45 (2001) 427.
[20] S. van Donk, A.H. Janssen, J.H. Bitter, K.P. de Jong, Catal. Rev. 45 (2003) 297.
[21] C.V. McDaniel, R.W. Baker, C.A. Rundell, US Patent 3595611 (1971), to W.R. Grace. &. Co.
[22] H.W. Beck, J.D. Carruthers, E.B. Cornelius, R.A. Kmecak, S.M. Kovach, W.P. Hettinger Jr., US Patent 4480047 (1984), to Ashland Oil Inc.
[23] S.M. Brown, G.M. Woltermann, US Patent 4235753 (1980), to Engelhard Minerals & Chemicals Co.
[24] S.M. Brown, V.A. Durante, W.J. Reagan, B.K. Speronello, US Patent 4493902 (1985), to Engelhard Co.
[25] L.B. Dight, D.C. Bogert, M.A. Leskowicz, US Patent 5023220 (1991), to Engelhard Co.
[26] E.I. Basaldella, R. Bonetto, J.C. Tara, Ind. Eng. Chem. Res. 32 (1993) 751.
[27] M. Xu, M. Cheng, X. Bao, Chem. Commun. 19 (2000) 1873.
[28] T. Rong, J. Xiao, Mater. Lett. 57 (2002) 297.
[29] Y. Han, N. Li, L. Zhao, D. Li, X. Xu, S. Wu, Y. Di, C. Li, Y. Zou, Y. Yu, F. Xiao, J. Phys. Chem. B 107 (2003) 7551.
[30] A.L. Yonkeu, V. Buschmann, G. Miehe, H. Fuess, A.M. Goossens, J.A. Martens, Cryst. Eng. 4 (2001) 253.
[31] R. Xu, W. Pang, J. Yu, Q. Huo, J. Chen, Chemistry–Zeolites and Porous Materials, Science Press, Beijing, 2004.
[32] R. Wang, L. Xu, L. Zhao, B. Chu, L. Hu, C. Shi, G. Zhu, S. Qiu, Microporous Mesoporous Mater. 83 (2005) 136.
[33] S. Wang, T. Dou, Y. Li, Y. Zhang, X. Li, Z. Yan, J. Solid State Chem. 177 (2004) 4800.
[34] J.C. Groen, W. Zhu, S. Brouwer, S.J. Huynink, F. Kapteijn, J.A. Moulijn, J. Perez-Ramirez, J. Am. Chem. Soc. 129 (2007) 355.
[35] M. Kruk, M. Jaroniec, Chem. Mater. 15 (2003) 2942.
[36] H. Liu, X. Bao, W. Wei, G. Shi, Microporous Mesoporous Mater. 66 (2003) 117.
[37] W. Guo, C. Xiong, L. Huang, Q. Li, J. Mater. Chem. 11 (2001) 1886.
[38] C. Belver, M.A.B. Munoz, M.A. Vicente, Chem. Mater. 14 (2002) 2033.
[39] A. Corma, M.S. Grande, V. Gonzalez-Alfaro, A.V. Orchillest, J. Catal. 159 (1996) 375.
[40] R. Le Van Mao, N. Al-Yassir, D.T.T. Nguyen, Microporous Mesoporous Mater. 85 (2005) 176.
[41] Y. Ooi, R. Zakaria, A.R. Mohamed, S. Bhatia, Appl. Catal. A 274 (2004) 15.
[42] M. Falco, E. Morgado, N. Amadeo, U. Sedran, Appl. Catal. A 315 (2006) 29.
[43] K. Miyazawa, S. Inagaki, Chem. Commun. 21 (2000) 2121.